Proceedings of the
Annual Stability Conference
Structural Stability Research Council
San Antonio, Texas, March 19-22, 2024

Flexural buckling tests on 1:4 scale wind turbine tower tubes

Dehui Lin[1], Anil Pervizaj[2], Søren Bøgelund Madsen[3], Andrew T. Myers[4]

Abstract

Wind energy is a growing source of renewable electricity across the globe. As the wind energy industry grows, the importance of optimization of wind turbine towers has increased. In particular, wind turbine OEMs aspire to minimize material usage of the tower, while maximizing annual energy production and minimizing costs. To achieve these goals, thin-walled steel tube sections are widely employed due to their efficient strength-to-weight ratio, cost-effectiveness and proven ability to be mass produced with sufficient quality. However, these sections, which typically have a large diameter-to-thickness ratio, are often limited in strength by their buckling resistance, a limit state that is sensitive to local geometric imperfections like dimples or weld depressions. Understanding the impact of these imperfections on the flexural buckling strength of tower sections is important to ensure their structural integrity and long-term performance. To address this issue, a series of static, flexural tests are conducted on a set of nine ~1:4 scale can-welded tubes with diameters of 1m and diameter-to-thickness ratios ranging from 150 to 300. Specimen geometries are selected to be scaled representations of common tube sections for wind turbine towers. A laser scanner is used to measure the geometries of the specimens before and during testing, enabling the characterization of initial imperfections and the evolution of deformation modes caused by local buckling. The preliminary results, including imperfection measurements, quality class categorization, and experimental results, are presented and discussed.

1. Introduction

The global shift towards wind energy as a renewable source of electricity source has been significant. The Renewables 2022 report by the International Energy Agency projects a growth in the global wind power capacity, encompassing both onshore and offshore wind power, of 42.4 gigawatts (GW) over the next five years, from 2022's 97.2 GW. This increase is approximately half of the existing capacity in 2022. This surge is fueled by the imperative to cut down greenhouse gas emissions through widespread deployment of clean energy technologies.

As part of this surge, the wind energy industry is working to construct more efficient wind turbine towers using less material. Wind turbine towers are carrying many loads, but an especially

---

[1] Ph.D. Candidate, Northeastern University, <lin.deh@northeastern.edu>
[2] Lead Engineer, Vestas Wind Systems A/S, < anpij@vestas.com >
[3] Lead Specialist, Vestas Wind Systems A/S, <sobgm@vestas.com >
[4] Professor, Northeastern University, <an.myers@northeastern.edu>

important load is overturning moment caused by wind thrust. Tower sections are typically fabricated from thin-walled steel tube sections, chosen for their efficient blend of strength, weight, ease of fabrication, and cost due to their high diameter-to-thickness ratios. However, their high diameter-to-thickness ratios or slenderness makes their strength limited by local buckling under compressive loading, especially when local geometric imperfections like dimples or weld depressions are present. Therefore, understanding the influence of these imperfections on the flexural buckling capacities of tube sections is essential for ensuring their structural integrity and long-term performance.

In the production of these steel tubes, a manufacturing process known as "can-welding" is frequently used. This method involves cutting steel plates to size, shaping them into cylinders or cones through plastic rolling, and then seam-welding them into “cans.” These cans are subsequently welded together circumferentially to create a tower section, with thick flanges welded at each end to connect sections to each other. This process introduces multiple geometric imperfections into the steel tubes, such as out-of-roundness, misalignments, and local imperfections like dimples. Research has extensively explored the impact of these imperfections on thin-walled tubes (e.g., Arbocz et al. 1969, Hutchinson et al. 1971, Berry et al. 2000). Their findings emphasize the importance of considering these imperfections to accurately assess the strength of thin-walled tubes under compressive stresses.

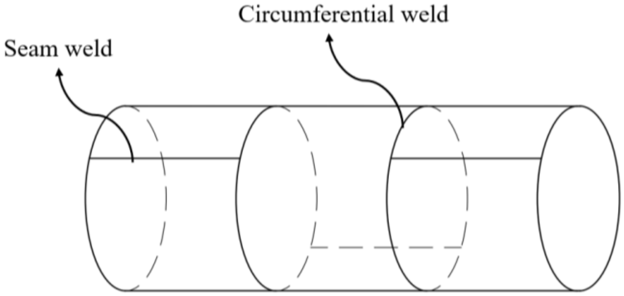

Figure 1: Schematic showing typical weld patterns for a can-welded tube section.

To address this concern, a series of quasi-static flexural tests are conducted on approximately quarter-scale can-welded tubes with 1 m diameters and diameter-to-thickness ratios ranging from 150 to 300, a range that is commonly used in wind turbine tower sections. A laser scanner is used to measure the specimens' geometric profile before and during testing to track initial imperfections and the development of local buckling deformation modes. The preliminary results, including imperfection measurements and characterization, and a comparison of maximum bending moments during tests with the design strengths specified in Eurocode EN 1993 1-6, are presented for discussion and analysis.

2. Experimental Program Overview

2.1 Objectives

This series of buckling tests has multiple objectives. First, the tests aim to assess the adequacy of current design guidelines for thin-walled tubes under flexural loading. There's a gap in experimental data for the flexural buckling capacities of structural components with these diameter-to-thickness ratios, especially when compared to data for tubes subjected to axial compression (Jay et al. 2016). This disparity underscores the need to evaluate existing design formulas.

Another key aspect of this research involves combining advanced scanning methods with large-scale experimentation. This approach allows for a comprehensive measurement of imperfections and a detailed examination of how these imperfections influence the buckling behavior of thin-walled steel tube sections. The outcome of this research is designed to provide insight into the structural characteristics of these tubes and support the development of enhanced design practices, especially finite-element-based design methodologies such as Geometrically and Materially Nonlinear Analysis with Imperfections (i.e., GMNIA) (Marques et al. 2013).

Presently, the dominant design standard for shell structures, EN 1993-1-6, proposes various methodologies for calculating the buckling strength of tower sections. One method uses empirically derived knockdown factors based on elastic critical stress, incorporating the impact of initial imperfections by categorizing tube sections into different fabrication quality classes. Another method involves the explicit modeling of imperfections using nonlinear finite element analysis. Both approaches require accurate imperfection measurements. This research addresses a significant gap, as data on imperfections for can-welded thin-walled tubes with varying diameter-to-thickness (D/t) ratios is scarce. The laboratory-scale tower section measurements in this study will provide useful data, enabling designers to refine design methods that more precisely account for imperfections in practical applications.

Lastly, the experimental testing of laboratory-scale specimens, combined with detailed imperfection measurements, is vital for validating computational models. This verification significantly boosts confidence in the use of computational modeling, leading to more reliable and efficient design approaches.

2.2 Summary of Specimen Geometry

This research involves the analysis of nine steel tube sections that are approximately 1:4 scaled representations of full-scale wind turbine tower section. These tubes are divided into three groups of varying thickness, with each group containing three nominally identical tubes. The nominal dimensions for each specimen are outlined in Table 1, which specifies the outside diameter D, thickness t and length L of the tubes. The naming convention for the specimens (e.g., CW-158-1) indicates the weld layout (CW for can weld), the D/t ratio (e.g., 158), and their order in the set of three replicates. Table 1 also presents the average yield stress, determined from at least four coupons extracted from the tubes following the bending test. The selection criteria for the coupon extraction regions were twofold: proximity to the neutral axis and avoidance of areas significantly impacted by testing.

Table 1. Summary of nominal dimensions and yield stress for all specimens.

Specimen	D [mm]	t [mm]	L [mm]	D/t	$f_{y,avg}$ [MPa]
CW-158-1/ CW-158-2/ CW-158-3	1003	6.35	3302	158	404
CW-211-1/ CW-211-2/ CW-211-3	1003	4.76	3302	211	445
CW-315-1/ CW-315-2/ CW-315-3	1003	3.18	3302	315	412

As shown in Fig. 2, each tube section includes 5 steel cylinders with equal thicknesses, three full lengths (825.5 mm) cans in the middle and two half-length cans (412.8 mm) on the ends. Two thick flanges (with thickness equal to 38.4 mm) are connected to the tubes at each end.

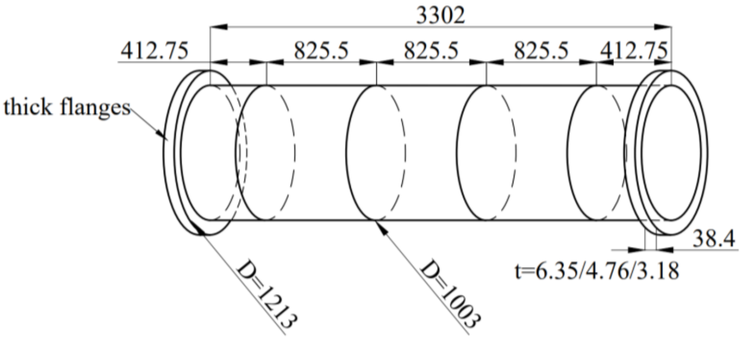

Figure 2: Nominal geometry of the tube sections, units in mm.

3. Testing Procedure

This section lays out the testing procedure used to assess the buckling strength of can-welded thin-walled steel tubes. The section includes a description of the experimental rig designed for this purpose, a summary of the pre-test imperfection measurement procedures, and finally a detailed description of the test procedure itself.

3.1 Rig Description

The flexural tests on the tube sections were carried out in Fall 2023 at the STReSS Lab at Northeastern University. A photograph of the test rig with a specimen installed is provided in Fig. 3. A schematic of the test rig is provided in Fig. 4.

Two hydraulic actuators were used to apply pure bending to each specimen by rotation of both ends of the specimen about two pins. The actuators each have capacities of 956 kN in tension and 1468 kN in compression, a stroke of ±381 mm and were positioned 2.4 m apart. The setup includes one pin in a slotted hole, allowing longitudinal displacements, but limiting transverse displacements, and another pin in a circular hole, restricting movement in both horizontal directions. The pure bending was achieved by contracting one primary actuator in displacement control and extending the other actuator for load control, matching the load in the primary actuator.

Each specimen was welded to a 38.1-mm-thick circular steel flange adapter on both ends, which in turn was welded to a 102-mm-thick, 1219 × 1219 mm square steel endplate with a partial joint penetration weld. No additional stiffening elements were added to the specimens. Each endplate was connected to a crossbeam made of W610 × 498, held together by 16 pre-tensioned 38.1 mm diameter threaded rods. To facilitate rotation, the crossbeams were placed on top of 16 305mm × 63.5mm ball bearing transfer plates at each support surface (4 plates per support surfaces), as shown in Fig. 5. Hardened steel 2.5mm thick steel plates are inserted above and below the ball bearings to prevent gouging of the mild steel cross-beams and support surfaces.

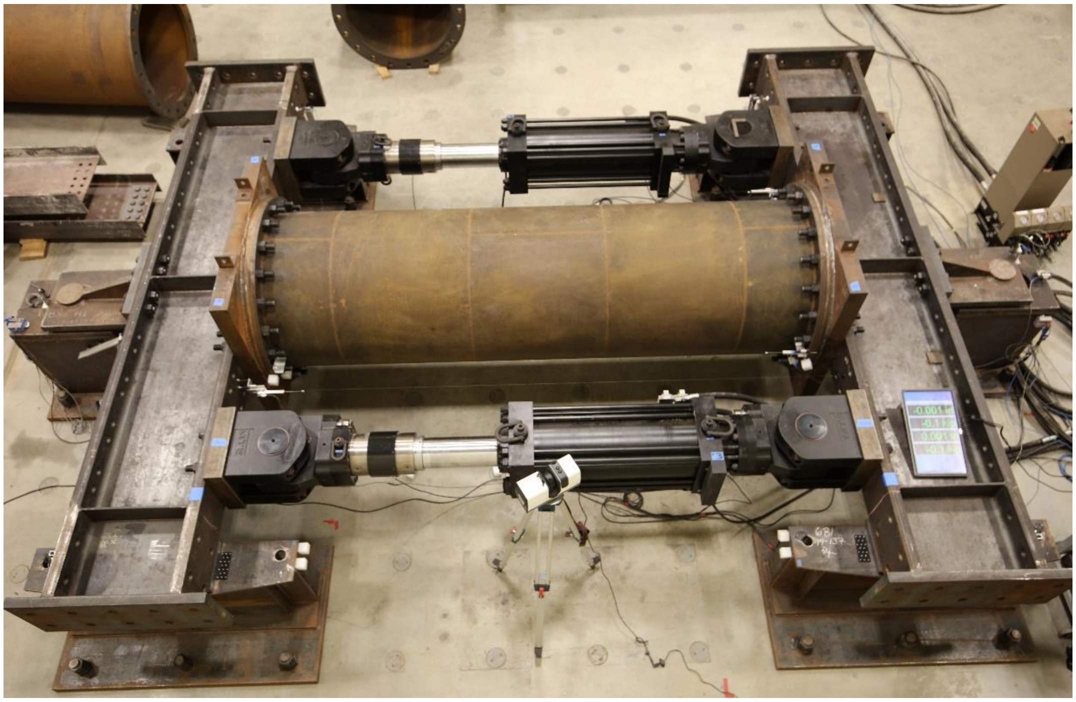

Figure 3: Photograph of experimental rig with one specimen installed.

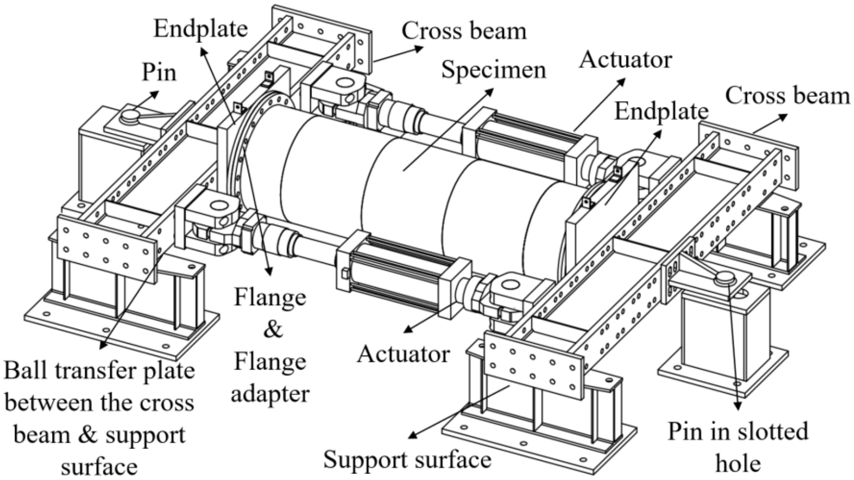

Figure 4: Schematic showing the experimental set-up for large-scale bending tests on can-welded tubes.

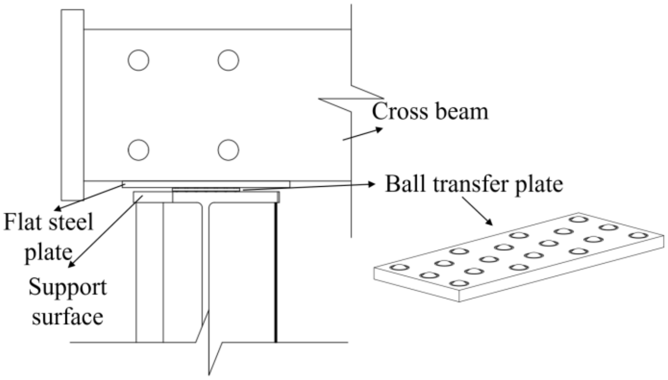

Figure 5: Positioning of ball transfer plates at the sliding interface between the cross beam and support surface.

3.2 Pre-Test Imperfection Measurements

This study uses a tripod-mounted 3D laser scanner to measure initial geometric imperfections. The scanning device has an angular accuracy of 25 arcsecs, a recommended working range of up to 50m, and a scanning speed of 208,0000 points/sec. Measurements were made on the outer surface of the tube. As shown in Fig. 6, during scanning, the tube was supported by the two thick end flanges, and placed on a platform, which elevates the bottom of the tube 635 mm above the ground. To capture the full-field geometric profile, six scans were conducted at six locations. These scans are sufficient to scan the entire surface of the tube sections with an incident angle (known to impact the scan data quality (Soudarissanane et al. 2011)) that did not exceed 70°, a requirement found in the literature (Lichti 2007) and supported by previous tests in the lab with the scanner. Scanning locations are plotted in Fig. 7. To align different scan samples from different locations, 35 white cube targets were used as reference points. The target locations were carefully designed to guarantee a minimum of six reference targets within the overlapping scanning area of two adjacent scans (e.g., scanner positions 1 and 2 in Fig. 7), meeting the scanner's requirements.

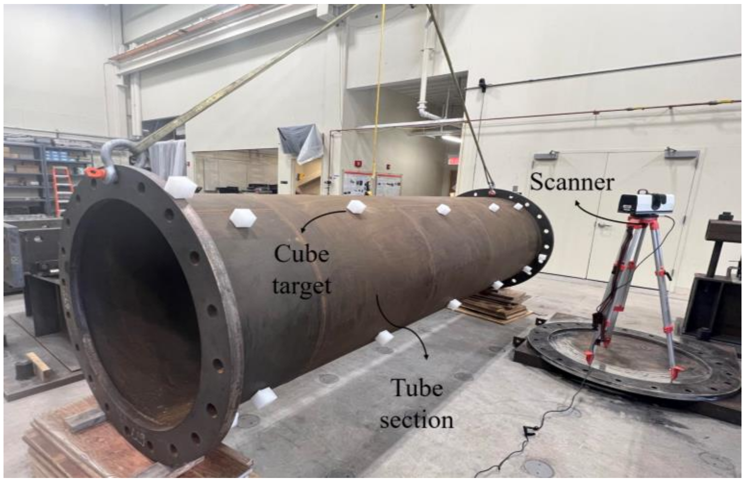

Figure 6: Picture of scanning setup.

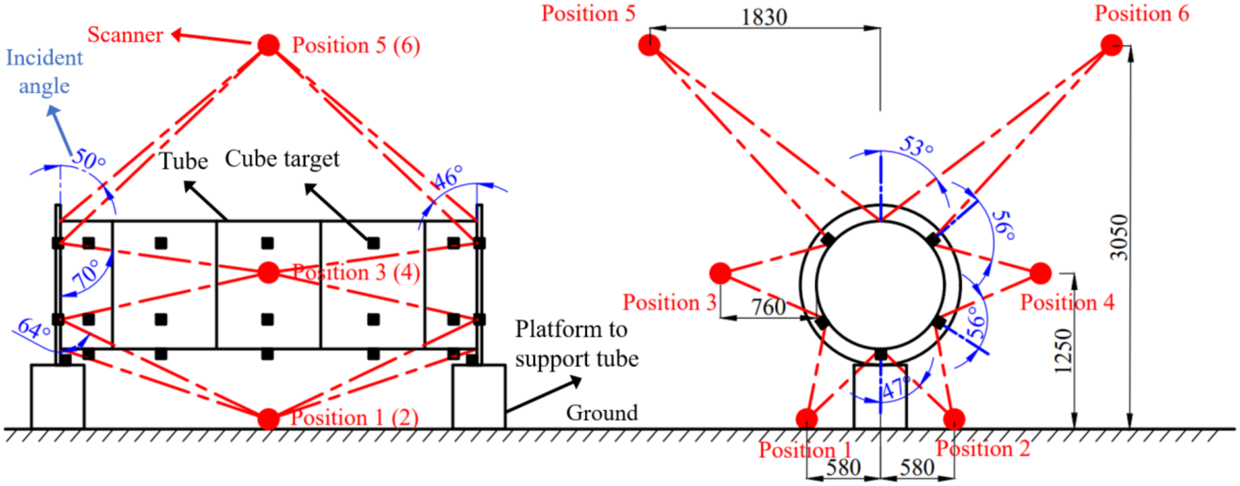

Front view

Side view

Figure 7: Illustration of the six scanner positions and 35 reference targets, unit in mm.

3.3 Test Procedures

As mentioned in Section 3.1, during the test, pure bending moment was applied with the primary actuator contracting in displacement control and the secondary actuator extending and matching the magnitude of force in the primary actuator. The contraction and extension of two actuators resulted in the rotation of the two cross beams, which in turn, causes the rotation of each end of the specimen. In addition, the slotted pin end allows any axial shortening of the specimen, avoiding the introduction of unintended axial force.

The evaluation of frictional forces due to the sliding of cross beams and the rotation of pins was conducted using two sets of small-amplitude load cycles (with θ_1=0.001 and θ_2=0.002 radians) prior to each experimental run. The hysteresis observed within these cycles provided a basis for estimating the frictional moments, which represent the discrepancy between the moments applied by the actuators (as recorded by actuator load cells) and those actually experienced by the test specimen. This estimation assumes that the friction observed during these initial cycles is indicative of friction levels throughout the testing procedure. This conceptual framework is illustrated in Fig. 8.

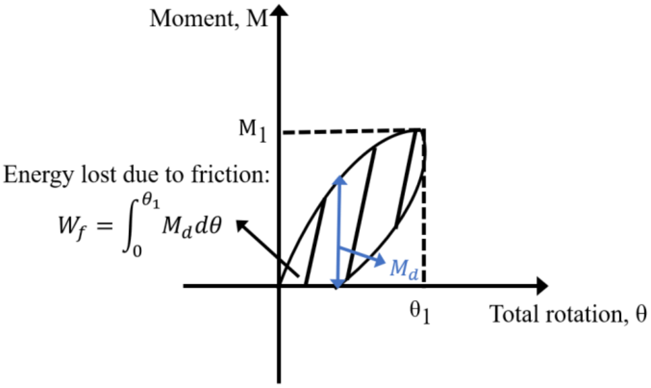

Figure 8: Estimation of frictional energy dissipation in small-Amplitude load cycles.

The hysteresis loop area was analyzed to approximate the frictional moments. The energy dissipated due to friction is quantified as $W_{f,1}=\int_0^{\theta_1} M_d d\theta$, where M_d is the difference in moments as measured by the actuators for an equivalent total rotation θ. The corresponding frictional moment is then calculated as $M_{f,1}=W_f/(2\theta_1)$. To ensure accuracy, the frictional moment M_f was determined by averaging the moments calculated from both sets of load cycles, given as $M_f=(M_{f,1}+M_{f,2})/2$.

The friction values obtained from various tests were consistent and varied according to the weight of the specimens. The heaviest specimen exhibited the highest friction value at 15 kN·m, the specimen of medium weight had a friction value of 7 kN·m, and the lightest specimen showed the lowest friction value at 4 kN·m.

After the friction estimated pre-test, the actuators were controlled to have of force under 0.44 kN. The displacement of the primary actuator was increased at a rate of 1.02-mm-per-minute, corresponding to a rate of total rotation, the sum of the two endplate rotations, of 0.02 degrees-per-minute. Except for the specimens that had weld fracture failure (CW-158-1 and CW-158-2), other tests were ended at approximately 1.7 degrees of total rotation of the specimens. Upon removal of the specimen from the rig, a final laser scan from the outside of the specimen was completed.

The test was regularly paused for scanning of the compressive region of the specimen or inspection of any areas of interest. The position for the scanner is plotted in Fig. 9 and Fig. 10. 140 degrees of the circumference were scanned and centered on the meridian of the tube under maximum compressive stress. The scanner was placed in two different positions for each pause. These scans provide measurements of the deformation of the compression face of the tube throughout the duration of the test, providing both a quantitative understanding of the progression of deformation through buckling and post-buckling.

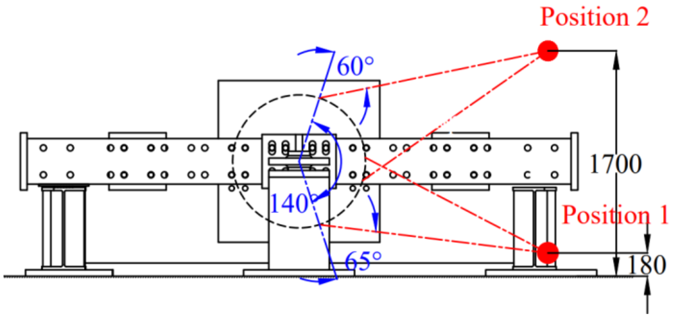

Figure 9: Schematic showing the scanner's positions during the tests (side view), unit in mm.

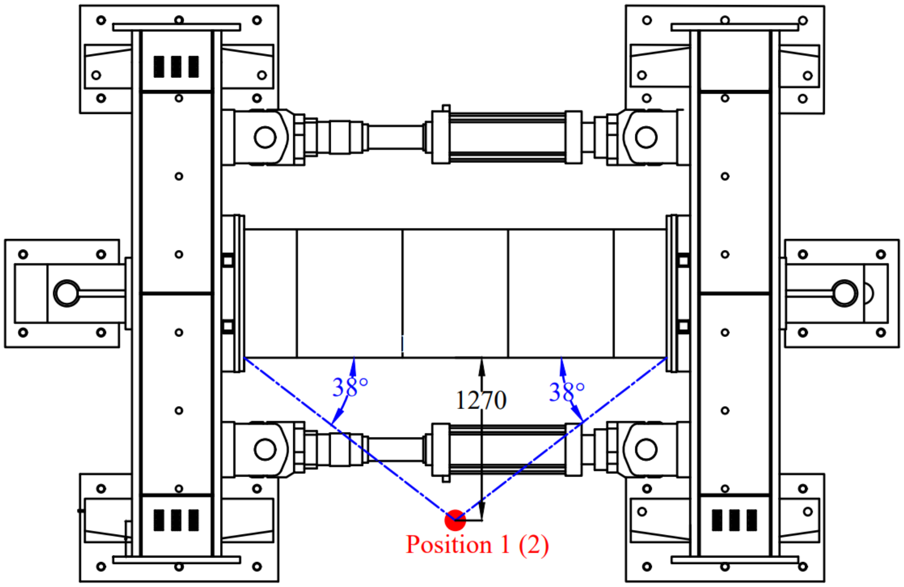

Figure 10: Schematic showing the scanner's positions during the tests (top view), unit in mm.

3.4 Instrumentation

All tests used the same instrumentation plan. In total, ten linear displacement transducers are used to measure displacements of the rig and specimen. The position of these LVDTs is plotted in Fig. 11, with corresponding description and names provided in Table 1.

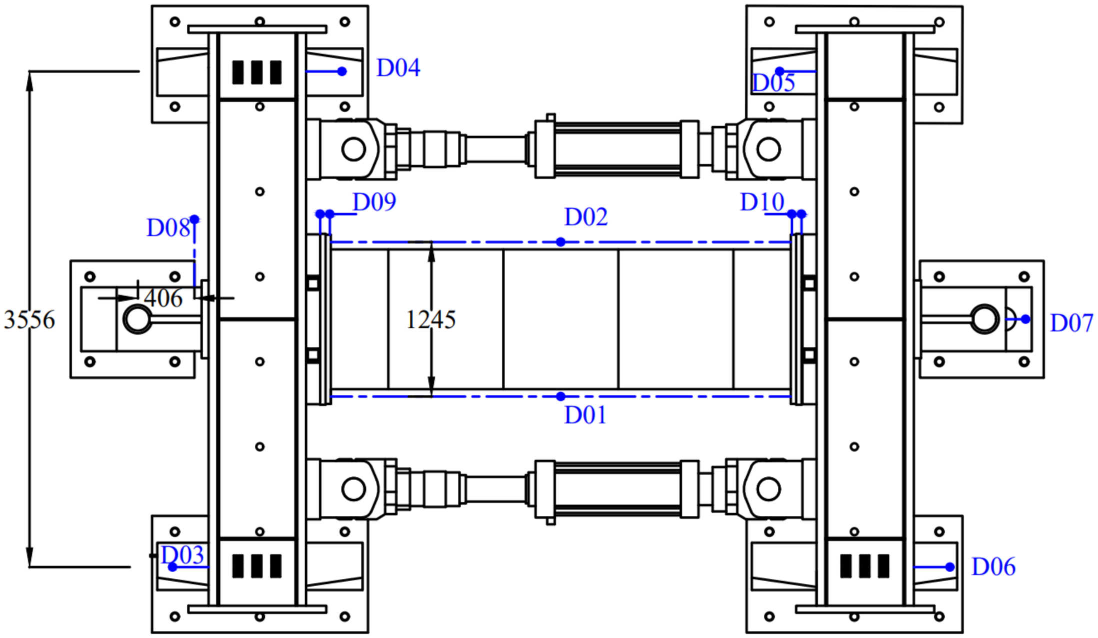

Figure 11: Schematic showing the position of the LVDTs used in the tests, unit in mm.

Table 1: Table listing the name and description of each sensor used in the tests.

Sensor Name	Description
AD3, AD4	Total displacements of actuators 3 and 4 measured by displacement transducers internal to the actuators
AF3, AF4	Force in actuators 3 and 4 measured by load cells internal to the actuators
D01, D02	Total axial displacement between endplates on the compression (D02) and tension (D01) side of the specimen
D03, D04	Linear displacement transducers use at each end of pin-side beam to measure rotation of the beam
D05, D06	Linear displacement transducers use at each end of slot-side beam to measure rotation of the beam
D07	Linear displacement transducer measurement of the axial deformation of the specimen measured at the back of the slotted pin assembly
D08	Linear displacement transducer measurement of rotation at the pin assembly
D09, D10	Linear displacement transducer measurement of the gap between the flange, flange adapters and cross beams

4. Preliminary Test Results

This section presents the results for CW-158-1, CW-211-3, and CW-315-3, including the measurement of initial imperfections, their quality class characterization, and a comparison between the maximum bending moment with the design strengths specified in Eurocode.

4.1 Imperfection Measurements and Characterization

4.1.1 Data Processing Method to Extract Geometric Imperfections

Geometric imperfections are calculated from the raw scan data using the following process. Flowchart of this process is presented in Fig. 12.

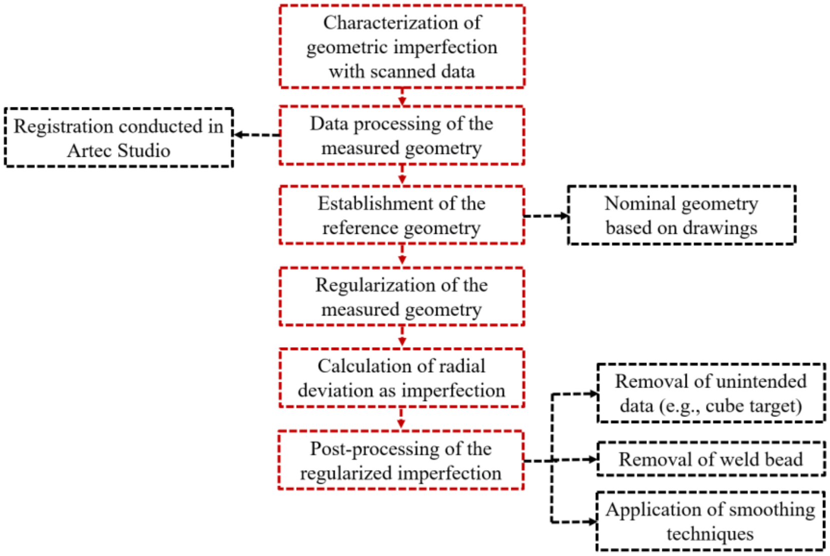

Figure 12: Flowchart showing the data processing method to extract geometric imperfections.

First, different scan samples from different locations are imported into Artec Studio, a commercially available point cloud analysis software provided by the scanner manufacturer. Each point cloud generated by the scanner at each location has its own coordinate system. The process of consistently aligning these diverse point cloud datasets into a unified model through coordinate transformation, is known as registration. Registration is conducted using the same commercial software with an algorithm that uses pairs of point sets (i.e., cube targets) to detect scan areas that should be aligned. After registration, one single point cloud with the full geometric profile of the specimen is obtained and exported.

The next step is to establish a reference geometry as the reference for calculation of imperfections. The reference geometry is selected using a numerical analysis to investigate the influence of gravity deformations. This revealed that gravity deformations are negligible compared to the magnitude of the measured imperfections. Therefore, the nominal geometry of the tube sections based on their drawings is selected as the reference geometry. The reference geometry is a structured point cloud with a resolution of 1mm both longitudinally and circumferentially. Once the measured geometry and the reference geometry are obtained, they are aligned using the "Iterative Closest Point" (ICP) (Wang et al. 2017) algorithm, which is designed to align two point clouds by minimizing the sum of squared distances between corresponding points.

The last step is the regularization of the measured geometry. The resolution of the measured geometry is about 0.5 mm and the resolution of the reference geometry is 1mm, which means the point cloud size of these two point clouds is different, making it impossible to directly calculate the deviations between two geometries. Through using closet point approach, for each point in the reference geometry, a closest point from the measured geometry can be found, and it is assumed that the imperfections are calculated as the differences between these two points. Basically, the regularization creates a subset from the measured geometry which has the same size as the reference geometry.

With the structured reference geometry, and the measured geometry with the same size, the differences between them can be calculated. In this study, it is assumed that all of the measured deviations are in the radial direction.

After calculating the radial deviations, three key steps are used to refine the regularized imperfection fields for analysis. Firstly, unintended data like cube targets are identified and removed, replacing their influence with average values from surrounding data points to maintain data integrity. Secondly, weld beads are removed due to their distortion effect on the scanning data. Data points within a 20 mm range from the weld centerline, typically the width of a weld bead, are excluded. Lastly, smoothing techniques are applied to the imperfection field to reduce noise and irregularities, enhancing suitability for Finite Element Analysis (FEA) as well as quality class classification. This involved using two filters: the 'non-local mean filter', which removes fine noise while retaining detail, and the 'box filter', a moving-mean method that clarifies the underlying imperfection patterns with a window width set at one two-hundredth of the specimen length.

4.1.2 Results of Geometric Imperfections

Fig. 13 shows the measured geometric imperfections of CW-158-1, CW-211-3, and CW-315-3 on an unrolled geometry, plotted with a common color scale. The x-axis represents the longitudinal position, and the y-axis represents the circumferential position ϕ, varying from $-\pi$ to π. Circumferential welds and seam welds are identified by dark blue lines. Color in the figure represents the relative magnitude of the radial imperfection, which is the ratio between the absolute value of the radial imperfections and the maximum imperfection, with a positive value indicating an outward imperfection (i.e., with a radius greater than the reference geometry's radius), and a negative value representing an inward imperfection.

In all three graphs, there are distinct bands of positive and negative values that repeat in the circumferential direction. For example, for the segment x/L=0.4~0.6, varying from θ=-180° to θ=180°, one can observe that CW-211-3 exhibits pronounced outward imperfections near θ=-180° and inward imperfections near θ=90°. This pattern points to a cyclical imperfection along the circumference.

Also, for each section, the intensity and distribution of the imperfections vary across the whole tube. In some, the imperfections are more localized, while in others, they are more widespread. For instance, within the range of x/L=0.4~1 and θ=-45°~45°, CW-158-1 shows clear overall inward imperfections, and near the region of x=0.4 and θ=90°, it has distinct localized inward imperfections.

Furthermore, it can be found that as the thickness decreases, or the D/t ratio increases, the maximum imperfection of the tube section increases. CW-315-3, which has the highest D/t ratio and the thinnest plate, has the largest maximum imperfection, while CW-158-1, which has the smallest D/t ratio and the thickest plate, exhibits the smallest maximum imperfection.

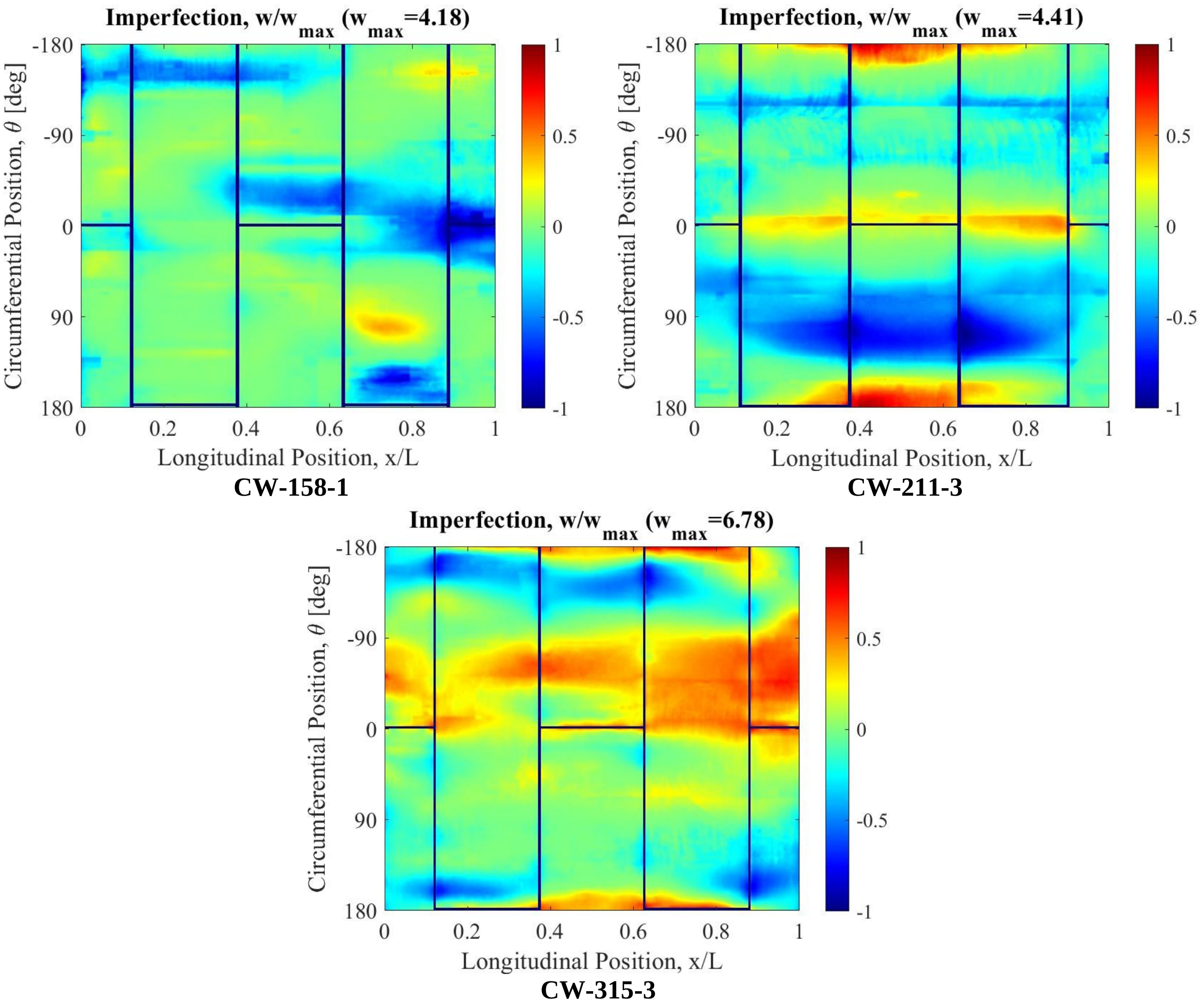

Figure 13: Radial imperfections of three tube sections, plotted with a common color scale.

4.1.3 Quality Class Classification

Eurocode EN 1993-1-6 provides a method for assessing the quality of shell structures like thin-walled tubes, for the purpose of calculating buckling capacities. This includes categorizing tube sections into different fabrication quality classes (A, B, or C) based on geometric imperfections, with class A being excellent quality, class B being high quality and class C being normal quality. The quality class classification involves measurement of three types of imperfection metrics: out-of-roundness, eccentricity, and dimple. These measurements are then compared against code limits to determine the tube's quality class. The out-of-roundness parameter U_r measures deviation from a perfect circle, while the eccentricity parameter U_e reflects the misalignment of two cross-sections near the circumferential welds from two adjacent cans. Dimples are localized imperfections like dents or weld depressions, categorized into weld and non-weld types, measured along different directions. Weld dimples are typically measured along longitudinal directions, and non-weld dimples are measured both along circumferential and longitudinal directions. Based on Eurocode provisions, the dimple parameter (U_{0x}, $U_{0\theta}$, U_{0w}) is defined as the maximum dimple depth over a defined gauge length, divided by the gauge length (l_{gx}, $l_{g\theta}$, l_{gw}).

With the regularized imperfection fields (as plotted in Fig. 13), three imperfection metrics can be calculated, and the results are provided in Table 2. Values for tolerances corresponding to each imperfection metric are provided in Table 3. The table provides the magnitude of the maximum imperfection and the corresponding quality class for each imperfection category individually and for all imperfections collectively (i.e., the worst quality class among all the imperfection categories). It's important to note that the defined quality class is based on the entire geometric profile of the specimen. However, during testing, the specimen undergoes pure bending, which subjects only half of its circumference to compression. Consequently, the most significant dimples may not be located within this compressive meridian. This results in a more conservative quality classification. Furthermore, the current method for categorizing quality class uses a laser scanner and considers the specimen's entire geometric profile. This is different from the conventional manual method outlined in EN 1993-1-6, which only measures specific locations on the specimen and is likely to miss the most severe deviations in roundness, eccentricity, and dimpling. Given this, the quality class categorization as per EN 1993-1-6 tends to be significantly conservative.

Table 2: Measurements of the maximum imperfection metrics and associated quality classes (QC) in EN 1993-1-6.

Specimen	EN 1993-1-6 Imperfections										Spec. QC
	Out-of-roundness		Eccentricity		Dimple						
					Longitudinal		Circumferential		Weld		
	$U_{r,max}$	QC	$U_{e,max}$	QC	$U_{x,max}$	QC	$U_{\theta,max}$	QC	$U_{w,max}$	QC	
CW-158-1	0.0065	A	0.0504	A	0.0061	B	0.0088	B	0.0057	A	B
CW-211-3	0.0106	B	0.1429	B	0.0086	B	0.0125	C	0.0092	B	C
CW-315-3	0.0161	C	0.2251	C	0.0134	C	0.0160	C	0.0095	B	C

Table 3: Values for tolerances corresponding to each imperfection metric in EN 1993-1-6.

Quality Class	Imperfection Metric		
	Out-of-roundness parameter * $U_{0r,max}$	Eccentricity parameter $U_{0e,max}$	Dimple parameter ($U_{0x,max}$, $U_{0\theta,max}$, $U_{0w,max}$)
Class A	0.009	0.14	0.006
Class B	0.013	0.20	0.010
Class C	0.020	0.30	0.016

* This value is calculated based on d = 1.003 m.

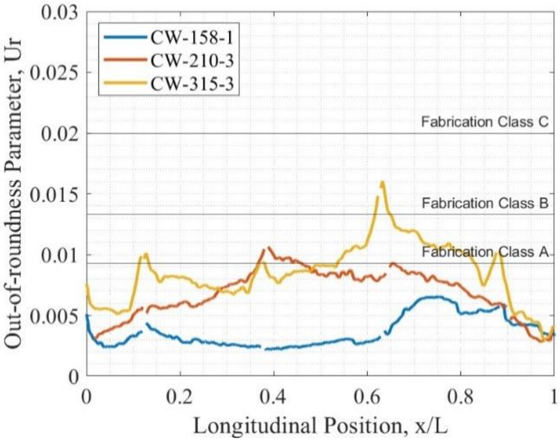

Figure 14: Out-of-roundness parameter U_r versus longitudinal position.

Fig. 14 shows the out-of-roundness parameter U_r in EN 1993 1-6 versus the axial position for CW-158-1, CW-211-3, and CW-315-3. In this figure, the EC limits for each quality class are shown by solid dark lines. Fig. 15 shows the most out-of-round cross section with imperfections magnified by 20 times in these three specimens. Blue lines show the cross sections of the measured geometries, and the red lines show the cross sections of the reference geometries. Black dashed lines indicate the axis of the seam welds.

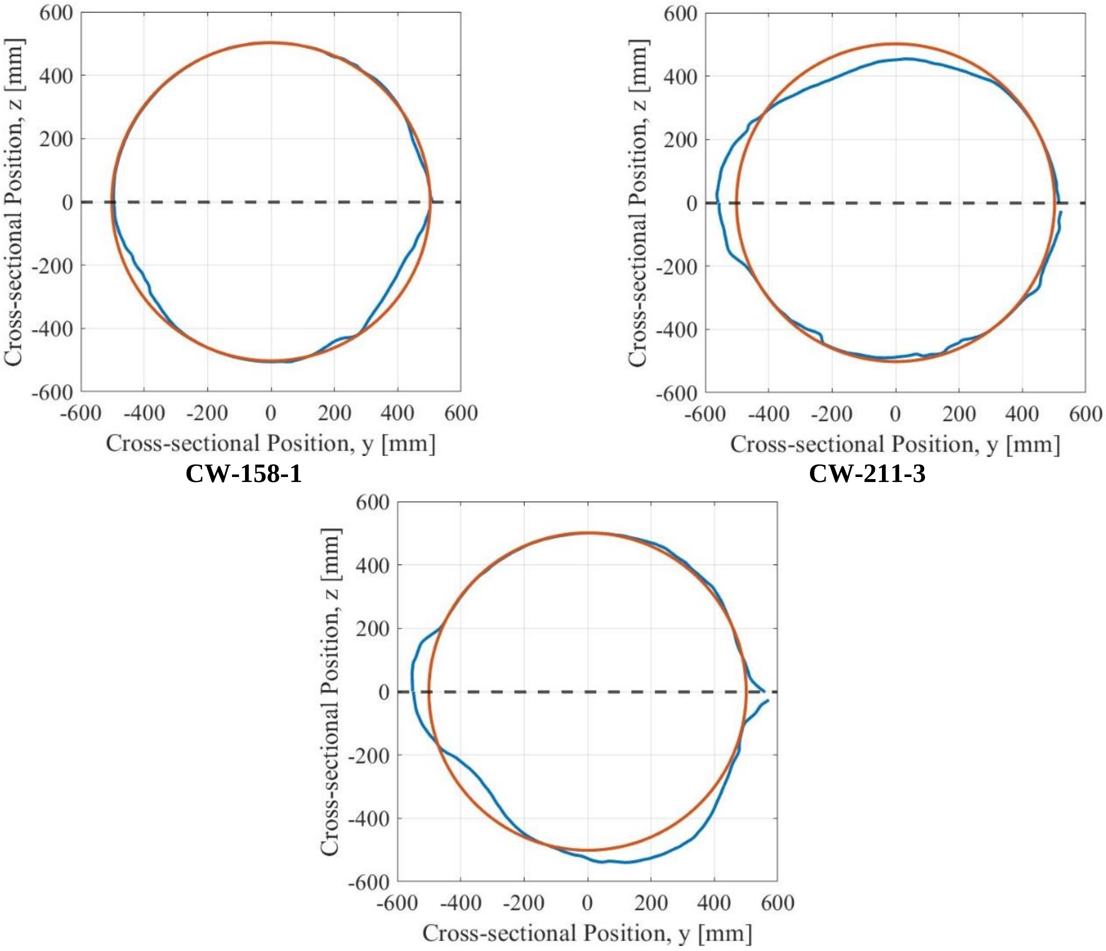

CW-158-1

CW-211-3

CW-315-3

Figure 15: The most out-of-round cross sections with imperfections magnified by 20 times. Blue lines show the cross sections of the measured geometries, and the red lines show the cross sections of the reference geometries. The black dashed line indicates the axis of the seam weld.

Fig. 16 illustrates the comparison between the centerlines of the measured and reference geometries for CW-158-1, CW-211-3, and CW-315-3, respectively, along the longitudinal axis, projected in the y and z axes, respectively. In each graph, the red dotted line denotes the centerline of the reference geometry, which is consistently at zero, representing the tube section's ideal shape. The blue line with markers represents the measured geometry's center point coordinates (y or z) for each cross-section. The red solid line is the fitted centerline of each can of the tube section, derived from the blue line's measurements. The vertical dashed lines indicate the positions of the circumferential welds. By analyzing the fitted centerlinethe differences between pairs of cross-sections at each side of the circumferential weld are computed and noted on the graphs. The figure is annotated with the numerical values of the angular misalignment, β, between adjacent cans (top line of text), and the eccentricity, e (bottom line of text), which is used to calculate the eccentricity parameter U_e, defined as the ratio of eccentricity e to thickness t.

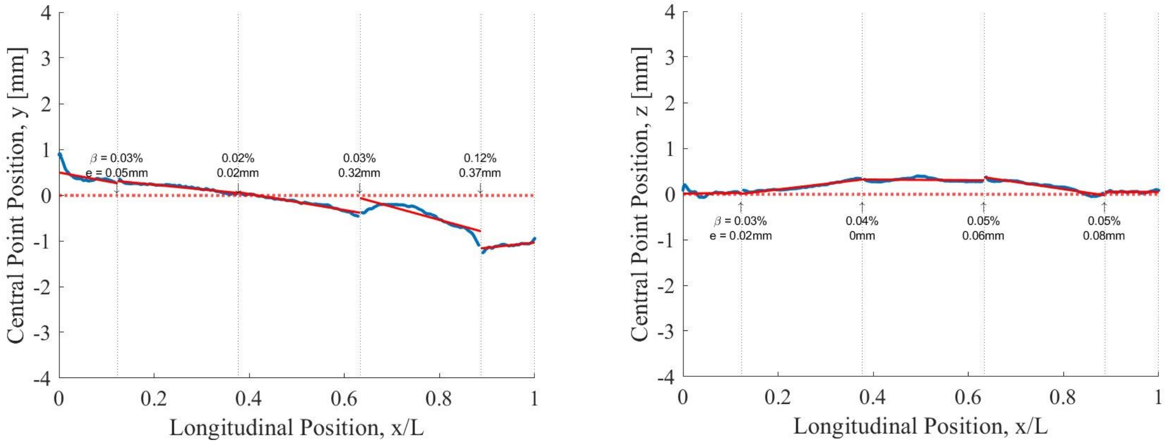

CW-158-1

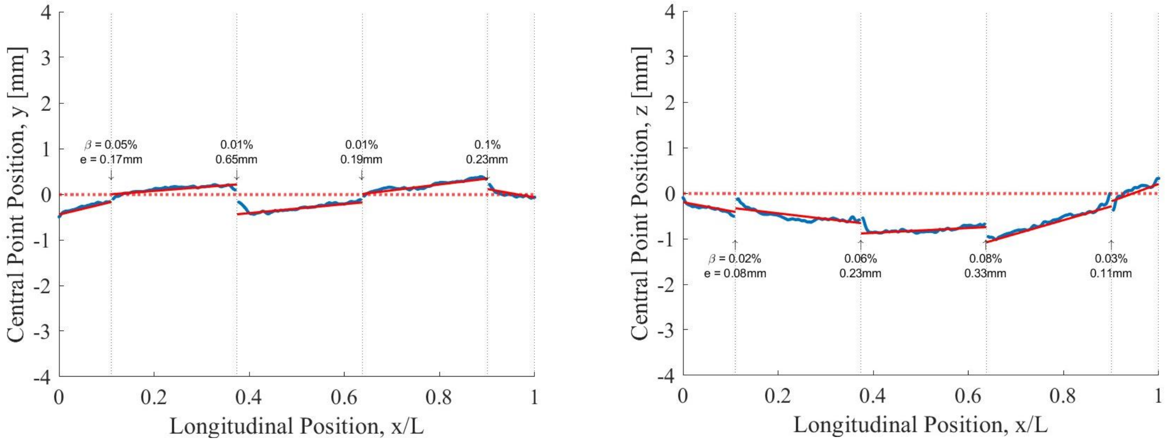

CW-211-3

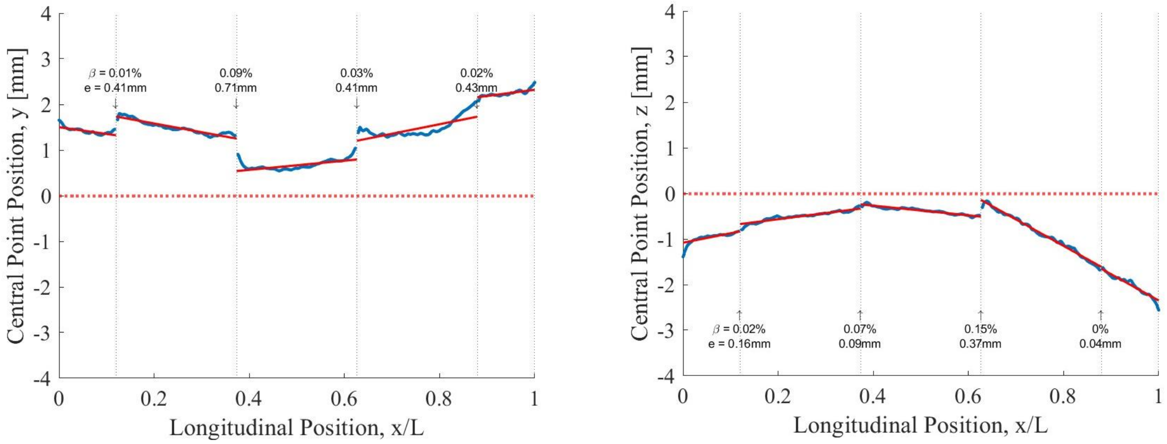

CW-315-3

(a) Y-direction (b) Z-direction

Figure 16: Comparison between the centerlines of the measured and reference geometries in (a) y-direction and (b) z-direction. The red dotted line denotes the centreline of the reference geometry. The blue line with markers represents the measured geometry's center point coordinates (y or z) for each cross-section. The red solid line is the fitted centerline of each can of the tube section, derived from the blue line's measurements. The vertical dashed lines indicate the positions of the circumferential welds. Text annotations indicate angular misalignment, β , between adjacent cans (top line of text) and the eccentricity, e (bottom line of text).

These graphs show a high degree of precision in the measured geometry, with only minor deviations from the reference geometry. The maximum eccentricity e observed in CW-158-1, CW-211-3, CW-315-3 are 0.32 mm (1/20 of the thickness), 0.65 mm (1/7 of the thickness), and 0.71 mm (1/5 of the thickness), respectively. These graphs do not indicate any systematic deviation that would suggest a pattern of imperfection; rather, the variations appear to be random.

Finally, Fig. 17 shows the profiles for the worst measured longitudinal dimples, the worst circumferential dimples and worst weld dimples for these three tubes. In each graph, the red line shows the deviations from the outer surface of the reference geometry, i.e., the imperfections. A direct blue line is drawn between the end points across the specific gauge length (l_{gx}, $l_{g\theta}$, l_{gw}). Subsequently, point with maximum distance to the straight blue line is identified and this distance is considered the depth of the dimple Δ_{max}. Next the dimple parameters (U_{0x}, $U_{0\theta}$, U_{0w}) are computed by dividing the depth of the dimple by the specific gauge length, and they are noted in the graphs. The weld bead, which results in an elevated area on the tube due to the added welding material, is represented by the shaded rectangle. As the scanning information from this weld bead area is compromised in precision, it is excluded from the displayed data in the graphs.

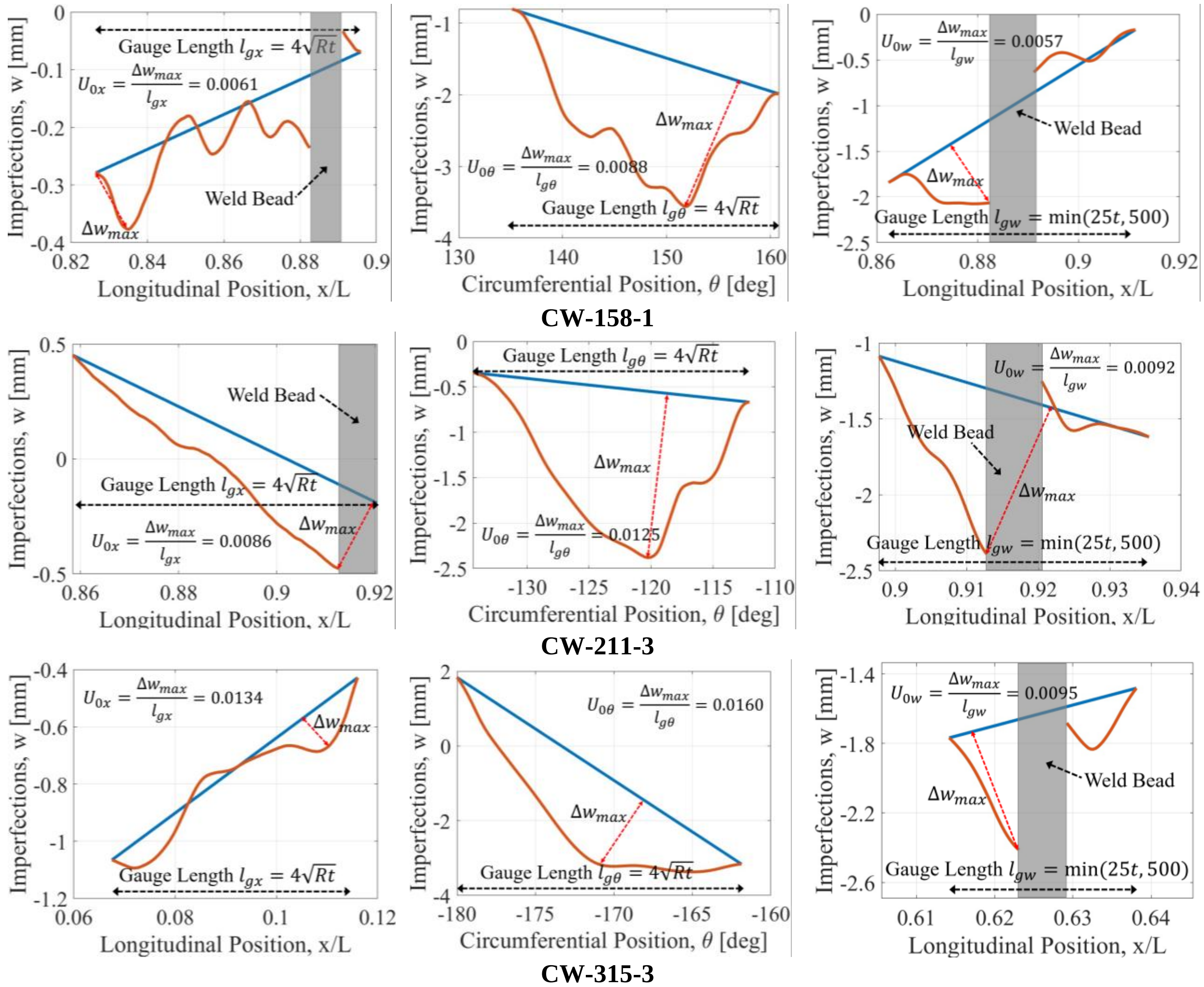

CW-158-1

CW-211-3

CW-315-3

(a) Worst Longitudinal Dimple (b) Worst Circumferential Dimple (c) Worst Weld Dimple

Figure 17: Profiles of (a) worst longitudinal dimple, (b) worst circumferential dimple, and (c) worst weld dimple.

4.2 Experimental Results

Table 4 shows the results from the flexural tests for CW-158-1, CW-211-3, and CW-315-3. Moment is calculated from force measurements taken from the load cells internal to the actuators, with moments reduced to account for friction, as described in Section 3.3. Except for CW-158-1, which has a weld fracture failure, the other two tests were ended when total rotation θ=0.03 radians. In Table 4, M_t is the peak moment immediately preceding the first load drop due to local buckling, θ_t is the total specimen rotation (measured with D01 and D02 as listed in Table 1) at M_t, M_y is the first yield moment for the tube section. Ratios between M_t/M_y are also given in the table.

Table 4: Summary of the flexural buckling results.

Specimen	M-θ at peak		Test to Design Code	
	M_t [kN·m]	θ_t [rad]	M_y [kN·m]	M_t/M_y
CW-158-1	1994	0.020	2019	0.99
CW-211-3	1522	0.017	1673	0.91
CW-315-3	918	0.012	1019	0.90

The results for each specimen are also plotted in Fig. 18. The dark solid line illustrates the relationship between the moment M and total rotation θ. Each graph also includes a comparison between the flexural stiffness (EI/L) calculated from test data and the theoretical flexural stiffness. Additionally, five dashed black horizontal lines represent the plastic moment M_p, first-yield moment M_y, and characteristic design capacity as predicted by the Eurocode's Stress Design procedure for quality class A, B, and C ($M_{SD\text{-}A}$, $M_{SD\text{-}B}$, $M_{SD\text{-}C}$).

Examining specimen CW-158-1, initial linear behavior is observed, with test-derived flexural stiffness closely aligning with theoretical values. Around 700 kN·m of moment (approximately one-third of the peak moment), the flexural stiffness starts to soften, indicating nonlinear behavior. The moment peaks at a rotation of 0.020, then rapidly decreases, maintaining roughly 80% of peak capacity. The moment continues to drop down upon further rotation until a weld fracture at 0.030 rad resulted in total capacity loss.

In the case of CW-211-3, a pattern similar to CW-158-1 was observed, starting with linear behavior. Nonlinear behavior initiates at a moment of 1000 kN·m (about two-thirds of the peak moment). The specimen buckled at a total rotation of 0.017 rad, leading to a significant moment drop to about 70% of peak capacity. As rotation increased, the buckling deformations increased, and the moment decreased slowly. The test was stopped when total rotation reached 0.030 rad.

For CW-315-3, the specimen maintained linear behavior up to the first load drop with minimal nonlinearity. It buckled at a total rotation of 0.012, causing the moment to drop sharply to around 50% of peak capacity. Its post-buckling behavior mirrored that of CW-211-3, with the buckling deformations increasing and the moment decreasing smoothly as rotation increased. This test also ended when the total rotation reached 0.030 rad.

Commonalities among the three cases include initial linear behavior and a rapid drop in moment due to buckling. However, they also exhibited distinct characteristics. Nonlinearity before the peak moment varied among the specimens, being clear in CW-158-1, moderate in CW-211-3, and minimal in CW-315-3. Furthermore, their post-buckling behaviors differed: CW-158-1 experienced weld fracture post-buckling, whereas CW-211-3 and CW-315-3 showed significant ductility after the rapid moment decrease.

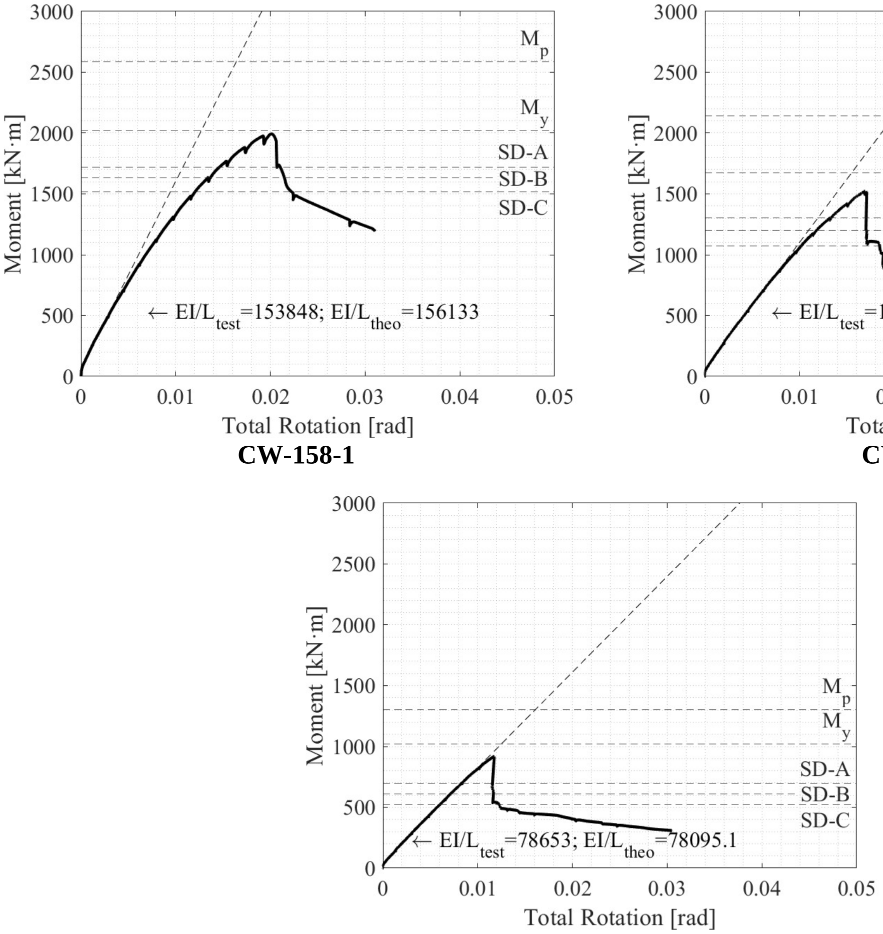

CW-158-1 **CW-211-3**

CW-315-3

Figure 18: Moment versus rotation behaviours.

Fig. 19 displays photographs of each specimen immediately after the initial load drop and at the test's conclusion for comparative analysis. In the case of CW-158-1, no notable changes are visible to the naked eye following the first load drop, with the final failure occurring at the slot end. For CW-211-3, after the first load drop, buckling is clearly observed at midspan of the specimen. By the end of the test, this buckling had expanded to encompass more than half the circumference. Similarly, CW-315-3 experienced midspan buckling after the first load drop, which intensified progressively during the post-buckling phase.

CW-158-1

CW-211-3

CW-315-3

(a) Photos taken immediately after the first load drop (b) Photos taken at the end of the test

Figure 19: Photographs of the region of the compressive region.

5. Discussions and Conclusions

In this study, experiments on three 1:4 scale can-welded, thin-walled steel tubes with D/t ratios of 158, 211, and 315, respectively were conducted. This research aimed to gather experimental data for thin-walled steel tubes with varying slenderness, which are not extensively studied. Gaining a deeper understanding of the strength and behavior of such cross-sections is crucial for enhancing existing design techniques and for the development of future computational design methods.

The paper details the imperfection measurements and test results of the three specimens. High-resolution 3D laser scanning was employed to measure the imperfections in these tubes, and a comprehensive method for analyzing the scan data was outlined. This method enables the characterization of geometric imperfections and facilitates the classification of tube sections into quality classes based on criteria such as out-of-roundness, dimples, and eccentricity.

Each test's results are described and analyzed in detail. A common trend observed in all three specimens was an initial linear response followed by a sudden decrease in moment due to buckling. However, each specimen exhibited distinctive characteristics. The nonlinearity was pronounced in CW-158-1, moderate in CW-211-3, and minimal in CW-315-3. Additionally, their responses post-buckling varied; CW-158-1 showed weld fracture post-buckling, while CW-211-3 and CW-315-3 demonstrated considerable ductility after the initial moment drop.

This research provides detailed imperfection profiles and experimental results. These contribute to the advancement of finite element-based design methods and offer insights for designers of structures like wind turbine towers. Future work will consider the correlation between the imperfections and the buckling capacities, as well as the buckling locations of the specimens. Furthermore, the impact of varying D/t ratios on failure modes requires more in-depth investigation. This continued research is important for a more comprehensive understanding of the behavior of thin-walled steel tubes with various D/t ratios and will significantly inform both practical applications and theoretical models in structural engineering.

Acknowledgments

The authors gratefully acknowledge the financial support of the US National Science Foundation through award #1912354 and award #1912481. Any opinions, findings, and conclusions or recommendations expressed in this material are those of the authors and do not necessarily reflect the views of the National Science Foundation. The assistance of Michael MacNeil, Nicholas Briggs, and Sujit Bhandari at Northeastern University is greatly appreciated.

References

Arbocz, J., & Babcock, C. D. (1969). The effect of general imperfections on the buckling of cylindrical shells. Journal of Applied Mechanics, 36(1), 28-38.

Berry, P., Rotter, J., & Bridge, R. Q. (2000). Compression Tests on Cylinders with Circumferential Weld Depressions. Journal of Engineering Mechanics, 405-413.

Hutchinson, J. W., Muggeridge, D. B., & Tennyson, R. C. (1971). Effect of a local axisymmetric imperfection on the buckling behavior of a circular cylindrical shell under axial compression. AIAA journal, 9(1), 48-52.

Soudarissanane, S., Lindenbergh, R., Menenti, M., Teunissen, P. (2011). “Scanning geometry: Influencing factor on the quality of terrestrial laser scanning points.” ISPRS journal of photogrammetry and remote sensing, 66(4), 389-399.

Jay, A., Myers, A. T., Torbian, S., Mahmoud, A., Smith, E., Agbayani, N., et al. (2016). Spirally welded steel wind towers: Buckling experiments, analyses, and research needs. Journal of Constructional Steel Research, 125, Pages 218-226

Lichti, D. D. (2007). “Error modelling, calibration and analysis of an AM–CW terrestrial laser scanner system.” ISPRS journal of photogrammetry and remote sensing, 61(5), 307-324.

Marques, L., Luís Simões da Silva, L. S., Greiner, R., Rebelo, C., Taras, A. “Development of a consistent design procedure for lateral–torsional buckling of tapered beams.” Journal of Constructional Steel Research, 89, 213-235.

Wang, F., Zhao, Z. (2017). “A survey of iterative closest point algorithm.” Chinese Automation Congress (CAC), pp. 4395-4399.